Bioactive Materials 10 (2022) 207–221

Contents lists available at ScienceDirect

Bioactive Materials

journal homepage: www.keaipublishing.com/en/journals/bioactive-materials

A bone-targeted engineered exosome platform delivering siRNA to treat osteoporosis

Yongzhi Cui [a,b,1], Yuanyuan Guo [c,1], Li Kong [d], Jingyu Shi [c], Ping Liu [e], Rui Li [b], Yongtao Geng [b], Weihang Gao [e], Zhiping Zhang [d], Dehao Fu [a,b,*]

[a] Department of Orthopedics, Shanghai General Hospital, Shanghai Jiao Tong University School of Medicine, Shanghai, 200080, PR China
[b] Department of Orthopaedics, Union Hospital, Tongji Medical College, Huazhong University of Science and Technology, Wuhan, Hubei, 430022, PR China
[c] Department of Pharmacy, Liyuan Hospital, Tongji Medical School, Huazhong University of Science and Technology, Wuhan, Hubei, 430077, PR China
[d] Tongji School of Pharmacy, Huazhong University of Science and Technology, Wuhan, Hubei, 430030, PR China
[e] Department of Orthopaedics, Liyuan Hospital, Tongji Medical College, Huazhong University of Science & Technology, Wuhan, Hubei, 430077, PR China

ARTICLE INFO

Keywords:
Exosomes
MSCs
siRNA
Bone targeting peptide
Osteoporosis therapy

ABSTRACT

The complex pathogenesis of osteoporosis includes excessive bone resorption, insufficient bone formation and inadequate vascularization, a combination which is difficult to completely address with conventional therapies. Engineered exosomes carrying curative molecules show promise as alternative osteoporosis therapies, but depend on specifically-functionalized vesicles and appropriate engineering strategies. Here, we developed an exosome delivery system based on exosomes secreted by mesenchymal stem cells (MSCs) derived from human induced pluripotent stem cells (iPSCs). The engineered exosomes BT-Exo-si*Shn3*, took advantage of the intrinsic anti-osteoporosis function of these special MSC-derived exosomes and collaborated with the loaded siRNA of the *Shn3* gene to enhance the therapeutic effects. Modification of a bone-targeting peptide endowed the BT-Exo-si*Shn3* an ability to deliver siRNA to osteoblasts specifically. Silencing of the osteoblastic *Shn3* gene enhanced osteogenic differentiation, decreased autologous RANKL expression and thereby inhibited osteoclast formation. Furthermore, *Shn3* gene silencing increased production of SLIT3 and consequently facilitated vascularization, especially formation of type H vessels. Our study demonstrated that BT-Exo-si*Shn3* could serve as a promising therapy to kill three birds with one stone and implement comprehensive anti-osteoporosis effects.

1. Introduction

Osteoporosis is a systemic skeletal disease characterized by low bone mass and microarchitectural deterioration of bone tissue, with a consequent increase in bone fragility and susceptibility to fracture [1]. It is well accepted that osteoclastic bone resorption exceeds osteoblastic bone formation, resulting in a decrease in bone mineral and consequent osteoporosis [2]. Thus, the current strategy for treating osteoporosis mainly focuses on suppressing osteoclast activity or inducing bone formation. Inhibitors of osteoclast differentiation and activation (e.g., oestrogen, selective oestrogen receptor modulators (SERMs), bisphosphonates, denosumab, and calcitonin) have been used in the clinic for many years. However, these drugs fail to restore osteoblast function and rebuild bone microarchitecture, while they can also cause many adverse effects [3,4]. Drugs that promote bone formation (e.g., parathyroid hormone (PTH), PTH related peptide (PTHrP) and strontium ranelate), also have different problems with long-term use. For example, abaloparatide and teriparatide (N-terminal and C-terminal fragment of PTHrP, respectively) may produce nausea, leg cramps and osteosarcoma. Strontium ranelate is toxic to the circulatory system and was withdrawn by the manufacturer in 2017 [3]. These side effects are largely because they cannot accumulate in the bone microenvironment and act on targeted cells [5]. Therefore, novel safe medications with bone-targeting ability need to be developed.

In previous years, the roles of vascularization in the pathogenesis of osteoporosis have attracted increasing attention, especially a newly-discovered vascular subtype (type-H vessels) which regulate growth of the bone vasculature, recruit osteoprogenitors and couple osteogenesis

Peer review under responsibility of KeAi Communications Co., Ltd.
* *Corresponding author. Department of Orthopedics, Shanghai General Hospital, Shanghai Jiao Tong University School of Medicine, Shanghai, 200080, PR China
E-mail address: fudehao@sjtu.edu.cn (D. Fu).
[1] Yongzhi Cui and Yuanyuan Guo contributed equally to this work.

https://doi.org/10.1016/j.bioactmat.2021.09.015
Received 28 June 2021; Received in revised form 27 August 2021; Accepted 6 September 2021
Available online 17 September 2021

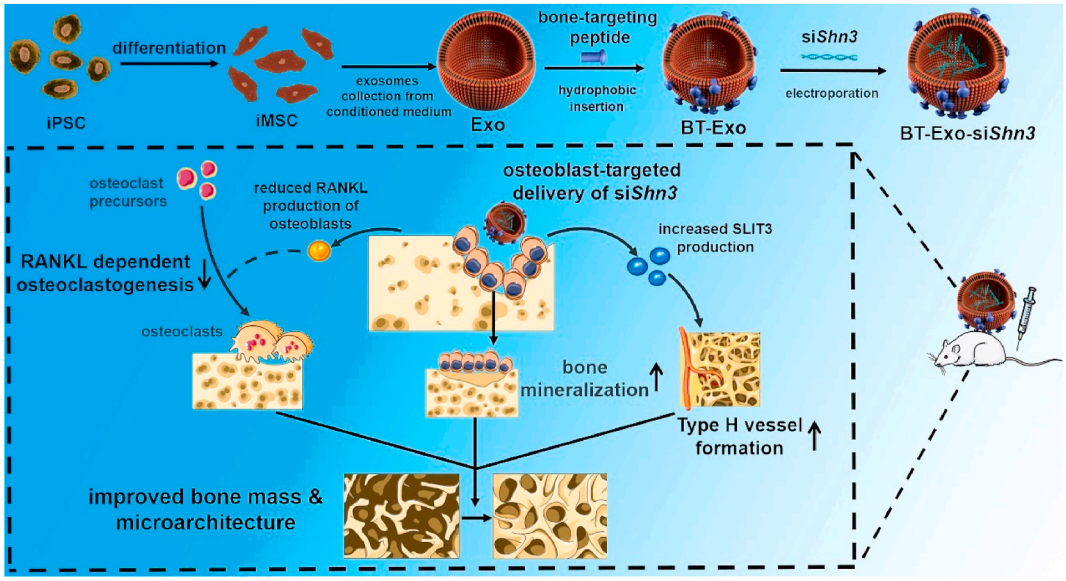

Scheme 1. Preparation of BT-Exo-si*Shn3* and the therapeutic mechanism.

to angiogenesis [6]. Recent studies revealed that the number of type-H vessels is apparently reduced in osteoporotic and aged bones, accompanied by a decrease in the number of osteoprogenitors [7,8]. Medications stimulating the formation of type-H vessels have been discovered to prevent bone loss to some extent [9,10]. In combination with these breakthroughs, we aim to develop a bone-targeting therapy for osteoporosis, which can inhibit bone resorption while promoting bone formation and vascularization.

Intimate temporal and spatial cross-talks exist between different types of bone cells, and one bioactive molecule may cause a cascade reaction, which can be developed as a therapeutic target. Schnurri-3 (SHN3) protein, encoded by the *Hivep3* gene (also called *Shn3* gene), inhibits osteogenic differentiation by suppressing ERK activity downstream of WNT signalling and promoting RUNX2 degradation [11,12]. In addition, SHN3 promotes osteoclast activity by facilitating receptor activator of nuclear factor-κB ligand (RANKL) expression by osteoblasts [13]. Furthermore, SHN3 inhibits the production of the proangiogenic factor slit guidance ligand 3 (SLIT3) and thus reduces type H vessel formation [14]. Previous studies have indicated that deletion of *Shn3* in mice completely prevents bone loss in an osteoporosis model, and short-term abrogation of SHN3 promotes bone formation in adult mice [15]. Thus, *Shn3* gene silencing could be a promising therapy, affecting osteoblasts, osteoclasts and type H vessels.

Exosomes, as natural extracellular vesicles (EVs), exhibit good biocompatibility and long-circulating ability [16]. Among them, MSC-derived exosomes have been proven to possess lower immunogenicity and higher levels of regenerative bioactive molecules compared to those with other cell origins [17,18], which may enhance the curative effects when the exosomes are used as delivery systems of exogenous medications [19,20]. Noticeably, a new subtype of MSCs, iMSCs (derivates of induced pluripotent stem cells (iPSCs)), incorporate the superiority of both MSCs and iPSCs. Billions of iMSCs can be generated from iPSCs, owing to their powerful self-renewal capacity, thus avoiding the invasive harvesting procedures required for conventional MSCs and the stemness decline with aging or cell passaging [21]. In addition, autologous iPSC-derived cells or their EVs can be used for treatment without raising ethical problems or immunological rejection, which may facilitate clinical application in the near future.

In this work, we constructed an engineered exosome delivery system BT-Exo-si*Shn3* based on exosomes of iMSCs (Scheme 1). The bone-targeting peptide modified with a diacyllipid tail was anchored onto the exosome membrane via hydrophobic interaction, and then the exosomes were loaded with siRNA of *Shn3* via electroporation. We found that (i) the exosomes possessed endogenous miRNA profiles of anti-osteoporosis gene expression, and the engineering procedures did not change the endogenous miRNA; (ii) BT-Exo-si*Shn3* could deliver siRNA to osteoblasts specifically and mediate osteoblastic *Shn3* gene silencing; and (iii) osteoblastic *Shn3* gene silencing enhanced osteogenic differentiation, promoted type H vessel formation and inhibited osteoclast formation, thus influencing all the major therapeutic mechanisms of osteoporosis. Overall, our data indicated that BT-Exo-si*Shn3* may represent a feasible and highly-effective cell-free therapy for osteoporosis, which may also provide new insight into targeted therapy for other bone diseases.

2. Materials and methods

2.1. Derivation of MSCs from iPSCs

Human iPSCs (cell line DYR0100) were routinely grown and proliferated on ESC-Qualified Matrigel (BD Biosciences, Franklin Lakes, NJ, USA) in mTESR1 (StemCell Technologies, Vancouver, Canada) in six-well plates [22]. When the cells were 80% confluent, the mTESR1 culture system was exchanged for an MSC differentiation medium kit (Nuwacell, China). After culture for 14 days in differentiation medium according to the protocols of the kit, the cells were digested with 0.25% trypsin-EDTA (Gibco/Life Technologies, Carlsbad, CA, USA) and then reseeded in 0.1% gelatine-coated 25-cm^2 culture flasks at a density of 5 $\times$ 10^4/mL in MSC culture medium (Nuwacell, Hefei, China). The cells were named Passage 1 upon reaching confluence. Generally, at Passage 3, they displayed a typical fibroblast-like morphology and were then used to analyse surface markers, differentiation capacity and for further experiments.

2.2. Cell culture

The mouse pre-osteoblast cell line MC3T3-E1 subclone 14, mouse ECs bEND.3, the Raw264.7 cell line and mouse BMSCs were obtained commercially from Procell Life Science & Technology (Wuhan, China). These cells were authenticated using the short tandem repeat method and proved negative for mycoplasma. Pre-osteoblasts were cultured in α-modified Eagle's medium (α-MEM) supplemented with 10% FBS, 100 IU/mL of penicillin, and 100 μg/mL of streptomycin. ECs were cultured in endothelial cell medium (ECM) (Cyagen Biosciences Inc., Guangzhou,

China) prepared according to the manufacturer's protocol. Raw264.7 cells were cultured in Dulbecco's Modified Eagle Medium (DMEM) supplemented with 10% FBS, 100 IU/mL of penicillin, and 100 μg/mL of streptomycin. Mouse MSCs were cultured in mouse MSC Medium (Cyagen) according to the protocol of the manufacturer. All cultured cells were maintained at 37 °C with 5% CO_2. The medium was replaced every 3 days, and the cells were reseeded into suitable flasks when reaching 70–80% confluence.

2.3. Exosome isolation and characterization

Exosomes were isolated from cell culture supernatant as described previously. Briefly, iMSCs were cultured in serum-free MSC medium for 48 h. Then the conditioned medium was harvested and centrifuged at 300×*g* for 8 min to remove non-adherent cells, then at 10^3×*g* for 15 min to remove dead cells and debris, and finally at 10^4×*g* for 60 min to remove large vesicles. Then the supernatant was transferred to an ultracentrifuge (Beckman Coulter, Brea, CA, US) and centrifuged at 10^5×*g* for 70 min. The cell pellet was resuspended with PBS and centrifuged at 10^5×*g* for another 70 min to remove contaminating proteins. All these steps were carried out at 4 °C. A BCA protein assay kit (Beyotime Institute of Biotechnology, Jiangsu, China) was used to measure the total protein concentration of the exosome suspension. NTA of exosomes Exo was performed using ZetaView (Particle Metrix, Meerbusch, Germany). DLS was performed using a Zetasizer Nano ZS90 (Malvern Instruments, Malvern, UK). The morphology was observed under a TEM (JEM-1200EX, JEOL Ltd., Tokyo, Japan) at a 100 keV accelerating voltage.

2.4. Animal care

Female C57BL/6 mice were obtained from the Experimental Animal Centre of Huazhong University of Science and Technology (HUST), China. All the mice were kept in specific pathogen-free (SPF) rooms in the animal centre. All animal care protocols and experiments involved in this study were in accordance with protocols approved by the Experimental Animal Centre of HUST. Twelve-week-old C57BL/6 female mice were randomly divided into six treatment groups (eight mice per group): sham, ovariectomy (OVX) alone, and OVX followed by treatment with BT-Exo, Exo-si*Shn3*, BT-Exo-si*Shn3*, or BT-Exo-siCon. These OVX groups were all performed with ovariectomy, while the sham group was removed some adipose tissues around the ovaries. After 6 weeks, experimental treatments were conducted. For each treatment group, 100 μL PBS containing 1.0 × 10^{11} particles per mL was intravenously injected once a week for 6 weeks through the tail vein. For the OVX alone group, 100 μL PBS was injected intravenously once a week for 6 weeks.

2.5. Synthesis of DSPE-PEG-Mal-Cys-SDSSD

The bone-targeting-peptide (98% purity assayed by HPLC) was synthesized by Wansheng Haotian Biological Technology (Shanghai, China) and dissolved in 5 mM Tris(2-carboxyethyl) phosphine hydrochloride (TCEP) solution at 1 mg/mL. Next, 1,2-distearoyl-*sn*-glycero-3-phosphoethanolamine-N-[methoxy(polyethyleneglycol)-2000]-maleimide (DSPE-PEG-Mal, 98% purity assayed by HPLC) was synthesized by Xi'an Rixi Biological Technology Company (Xi'an, China) and dissolved in 5 mM HEPES buffer at 1 mg/mL. Then DSPE-PEG-Mal was reacted with the peptide in a molar ratio of 1:1 at room temperature for 24 h to prepare DSPE-PEG-Mal-Cys-SDSSD. The mixture was dialyzed against distilled water in a dialysis bag (molecular weight cutoff of 3000 Da) for 24 h. Finally, the solution after dialysis was freeze-dried and the DSPE-PEG-Mal-Cys-SDSSD powder was stored at −20 °C.

2.6. Modification of Exo with bone-targeting peptide

To combine Exo with bone-targeting peptide, 10 μL Exo (10^{12} particles/mL) and 90 μL of the DSPE-PEG-Mal-Cys-SDSSD (10 μM) were gently added into 100 μL PBS, and the mixture was incubated overnight at 4 °C. To remove uncombined DSPE-PEG-Mal-Cys-SDSSD, the mixture was washed with PBS by ultracentrifugation at 10^5×*g* at 4 °C for 70 min and resuspended in PBS. To confirm the successful modification of Exo, we combined the peptide labelled with fluorescein isothiocyanate (FITC) and captured the FITC-labelled Exo with immunomagnetic beads as described below.

2.7. Loading of small RNA into BT-Exo by electroporation

First, 10 μL BT-Exo (10^{12} particles/mL) and 100 μg siRNA/miRNA were lightly mixed in 400 μL of cold electroporation buffer (21% Opti-MEM™ reduced serum medium, 1.15 mM pH 7.2 potassium phosphate, 25 mM potassium chloride) and electroporated in a 4 mm cuvette by the electroporation apparatus using a 0.35-s pulse 20 times at 0.7 kV as previously described [23,24]. Then we incubated the mixture at 37 °C for 30 min to recover the complete membrane structure. To remove free siRNA/miRNA, the mixture was washed with cold PBS twice by ultracentrifugation at 10^5×*g* at 4 °C for 70 min and resuspended in PBS.

2.8. Identification of siRNA loading into BT-Exos by immunomagnetic bead capture

The Cy3-labelled siRNA was loaded into the BT-Exo by electroporation. The BT-Exo-si*Shn3*-Cy3 were incubated with immunomagnetic beads conjugated with CD63 antibodies at 37 °C for 30 min. Fluorescence microscopy (Olympus IX71, Tokyo, Japan) was used to analyse the fluorescent signal.

2.9. Evaluation of loading efficiency into BT-Exo

The evaluation of loading efficiency of siRNA/miRNA by electroporation was performed as described previously [24]. Briefly, miRNA of *Caenorhabditis elegans*, cel-miR-67, was loaded into BT-Exo. We divided the mixture into two halves and added RNase to one half at 37 °C for 30 min to decompose the miRNA absorbed onto the surface of BT-Exo; the counterpart without RNase added was used as a control. Each sample was treated with Trizol reagent (Invitrogen, Carlsbad, CA, USA) to extract total RNA and aliquots of cel-miR-39 were then introduced into the lysed samples as control for normalization. Q-PCR was used to quantify the RNA samples as mentioned below. To address the question of whether electroporation may cause siRNA/miRNA aggregation and that the aggregations may tolerate RNase, equal amounts of cel-miR-67 without BT-Exo was used for electroporation as a negative control and analysed as stated previously. Loading efficiency of siRNA/miRNA was calculated as (%) = $(R_{after\ digest} - R_{control})/(R_{before\ digest})$ × 100. In this calculation, $R_{after\ digest}$ was the amount of cel-miRNA-67 in the group treated by electroporation and RNase digestion; $R_{before\ digest}$ was the amount of the cel-miRNA-67 in the group treated by electroporation but without RNase digestion; $R_{control}$ was the amount of aggregated cel-miRNA-67 in the control group after RNase degradation.

2.10. Serum stability assay

To confirm the serum stability of the siRNA delivery system, free siRNA, Exo-siRNA or BT-Exo-siRNA were incubated with 50% FBS. Aliquots of different incubation times from each group were subject to electrophoresis on an agarose gel and then observed on a UV illuminator.

2.11. Cytotoxicity assays in vitro

CCK-8 assay was conducted to evaluate cell viability. Cells were incubated with Exo, BT-Exo, or BT-Exo-si*Shn3* at different concentrations. After treatment for 24 h, cell viability was examined using a CCK-8

kit according to the protocols.

2.12. miRNA sequencing

Total RNA of Exo and BT-Exo-si*Shn3* was extracted using Trizol reagent according to the manufacturer's protocols. Then the samples were sent to Cloud-seq Biotech (Shanghai, China) for high-throughput sequencing. Briefly, the purity and quantity of total RNA were analysed using a Nanodrop ND-100 (Thermo Fisher Scientific, Waltham, MA, USA). The miRNA sequencing library was prepared with total RNA of each sample, and ~150 bp PCR amplicons (corresponding to ~22 nt miRNAs) were selected. The libraries were then used for RNA sequencing with an Illumina HiSeq sequencer (Illumina) routinely [25].

2.13. Cellular uptake of Exos in vitro

Cellular uptake was assessed using flow cytometry and confocal laser scanning microscopy (CLSM). MC3T3-E1 cells were seeded into observation dishes for CLSM, at a density of 1×10^4 cells/dish. After the cells reached 80% confluence, the medium was exchanged for α-MEM containing Exo or BT-Exo labelled with DiR iodide at 37 °C. After treatment for 4 h, the supernatant was carefully removed. For CLSM analysis, the cells were gently washed three times with PBS and fixed with 4% paraformaldehyde for 15 min. Then the cells were washed another three times, stained using 4′,6-diamidino-2-phenylindole (DAPI) for 10 min, and ultimately observed under CLSM (Leica TCSNT1; Leica Microsystems Ltd, Wetzlar, Germany).

2.14. Biodistribution of BT-Exos in vivo

Each mouse was injected intravenously with DiR-labelled Exo or BT-Exo at a dose of 1 mg/mL and 0.2 mL. After different time intervals, the mice were euthanised. We isolated the major organs (brain, heart, liver, spleen, lung, kidney and long bones) to analyse the fluorescence intensity using Bruker Xtreme (Bruker Corp., Billerica, MA, USA, Germany).

2.15. Cell-specific delivery in vivo

Femurs of each mouse were dissected and decalcified using 10% EDTA for 3 days. After dehydration in 20% sucrose solution for 24 h, femurs were embedded in optimal cutting temperature compound (OCT; Sakura Finetec USA, Torrance, CA, USA) and cut into 10-μm sections. Histological analysis of femur sections from the different groups was used to evaluate cell-selective delivery efficiency. Green fluorescence signals indicating FAM-siRNA localization were observed under a fluorescence microscope. An *anti*-OCN monoclonal antibody (Abcam, Cambridge, MA, USA) at a 1:500 dilution and a Cy3-labelled secondary antibody at a 1:1000 dilution were used for labelling osteoblasts. DAPI was used to locate the cell nucleus.

2.16. Enzyme-linked immunosorbent assay (ELISA)

The levels of SLIT3, RANKL, osteoprotegerin (OPG), vascular endothelial growth factor (VEGF), tartrate resistant acid phosphatase 5b (TRAP5b), C-terminal cross-linking telopeptide of type-1 collagen (β-CTX), procollagen type-1 N-terminal propeptide (P1NP) and angiogenin in the supernatant were measured using ELISA kits (SLIT3, MU30961; RANKL, MU30342; OPG, MU30199; VEGF, MU30236; TRAP5b, MU30923; β-CTX, MU30091; PINP, MU30602; Bio-Swamp, Wuhan, China; angiogenin, ab208349, Abcam) performed in accordance with the manufacturers' protocols.

2.17. Tube formation assay

The mouse endothelial cells bEND.3 were reseeded onto Matrigel-coated 96-well plates and cultured in mixed medium. After 6 h, the ECs were stained with calcein–AM at 37 °C for 15 min. Each plate was observed and photographed under a fluorescence microscope.

2.18. Osteoblast and osteoclast coculture assay

Osteoclast precursors Raw264.7 cells and pre-osteoblasts MC3T3-E1 cells were used to simulate osteoblast-induced osteoclastogenesis using a transwell assay. MC3T3-E1 cells were seeded into the upper chamber, while Raw264.7 cells were cultured in the lower. The pore size of the polycarbonate membrane was 0.4 μm, so the secreted factors were able to pass through but the cells were restricted. The cultures in the upper chamber were supplemented with 10 nM $1,25(OH)_2D_3$ (Aladdin Chemistry Co., Ltd., Shanghai, China) and 1 μM PGE_2 (Aladdin) to induce RANKL expression of MC3T3-E1 cells [26]. BT-Exo-si*Shn3* and its counterparts were also supplemented into the upper chamber. After 8 days, TRAP staining (Sigma, St Louis, MO, USA) of the lower chamber cells was performed according to the manufacturer's instructions. The effect on osteoclastogenesis was measured by calculating the TRAP-positive area as a proportion of the total area. The F-actin ring assay was also performed to evaluate the osteoclastogenic effects. Briefly, the cells in the lower chamber were fixed in 4% paraformaldehyde for 10 min and then washed 3 times using PBS. This was followed by staining with Alexa Fluor 555 phalloidin for 1 h and DAPI staining for 15 min, then the cells were observed under a fluorescence microscope.

2.19. qRT-PCR

Cells were harvested and treated with Trizol reagent, and total RNA was obtained according to the supplier's protocols. A NanoDrop-2000 spectrophotometer (Thermo Fisher Scientific) was used to determine the concentration of RNA. Then miRNA samples were reverse transcribed using a stem-loop reverse transcriptase primer kit (Ribobio, Guangzhou, China). qRT-PCR was conducted with a SYBR Prime Script kit (Takara Bio Inc., Shiga, Japan) in triplicate. The comparative Ct ($2-\Delta\Delta Ct$) method was used to determine the relative expression difference.

2.20. Western blot analysis

A protein extraction kit (Beyotime) was used to isolate the total proteins from harvested cells in accordance with the protocols provided by the manufacturer. Equal amounts of protein sample were loaded and separated by SDS-PAGE, then transferred to 0.22-μm polyvinylidene difluoride (PVDF) membranes. The membranes were blocked with 5% skimmed milk and incubated using specific antibodies overnight. The primary antibodies used were: Alix (1:1000), CD81 (1:1000), CD63 (1:1000), NFATc1 (1:800), c-Fos (1:800), β-actin (1:1000), GAPDH (1:1000) (all from Abcam); SHN3 (1:1000) (Abnova, Taipei, Taiwan). Finally, we incubated the membranes with horseradish peroxidase (HRP)-labelled secondary antibodies for 1 h at room temperature.

2.21. Osteogenic induction and evaluation

MC3T3-E1 cells were reseeded into 12-well plates at a density of 2×10^4 cells per well. After 24 h, the medium was exchanged for α-MEM supplemented with osteogenic induction factors (10 nM dexamethasone, 5 mM β-glycerophosphate and 50 μg/mL ascorbic acid). In all cultures the medium was changed every 3 days. Alizarin red staining (ARS) and Alkaline Phosphatase (ALP) activity assay were used to assess the osteogenic effect. For the ALP activity assay, the cells were treated for 7 days. Briefly, the cells were washed gently four times using PBS and fixed in 4% paraformaldehyde for 15 min, then evaluated using an ALP assay kit (Beyotime) in accordance with the manufacturer's protocol. For ARS, the cells were treated for 14 days. After washing and fixing as

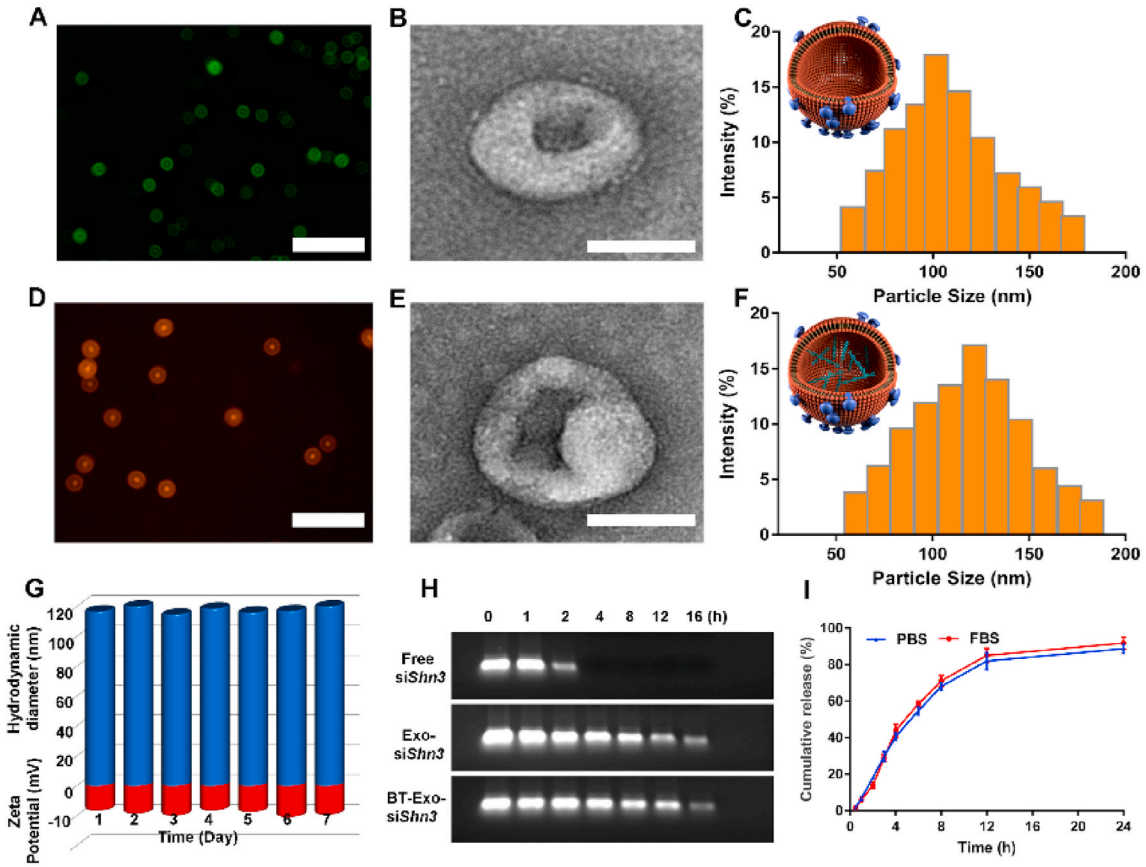

Fig. 1. Preparation and characterization of BT-Exo-si*Shn3*. Fluorescence images of (A) BT-Exos and (D) BT-Exo-si*Shn3* captured by immunomagnetic beads. Scale bar = 50 μm. TEM images of (B) BT-Exos and (E) BT-Exo-si*Shn3*. Scale bar = 100 nm. Size distribution of (C) BT-Exos and (F) BT-Exo-si*Shn3* measured by DLS. (G) Stability of hydrodynamic diameter (blue) and zeta potential (red) of BT-Exo-si*Shn3*. (H) Serum stability of Exo-si*Shn3*, BT-Exo-si*Shn3* and free si*Shn3* analysed by gel electrophoresis. (I) Release kinetics of si*Shn3* from BT-Exo-si*Shn3* incubated in PBS or FBS at 37 °C for 24 h (n = 3). (For interpretation of the references to colour in this figure legend, the reader is referred to the Web version of this article.)

above, the cells were stained with 2% Alizarin red (Sigma) for 15 min and washed gently with PBS. Each plate was observed and photographed under a fluorescence microscope. For quantitative analysis, 10% acetic acid was added to the cells. After incubation for 12 h, the mixture of cells and acetic acid was centrifuged for 10 min at 18,000×*g*, then the supernatant was removed and neutralized with 10% ammonium hydroxide. Finally, 100 μL of each sample was removed to a well of a 96-well plate and the absorbance was measured at 405 nm using a microplate reader [27].

2.22. Immunofluorescence staining of osteoblasts

The osteoblasts incubated with different nano-particles were fixed with 4% paraformaldehyde for 30 min at 20 °C. After permeabilization in 0.2% Triton X-100 for 8 min, osterix and osteocalcin were stained using the respective antibodies (OSX and OCN, Servicebio, China), then 5% BSA was used to block nonspecific binding. The primary antibodies of OSX and OCN were then incubated with the secondary antibodies labelled with Cyanine 3 (Cy3, Servicebio, Wuhan, China). DAPI (blue) and FITC-labelled phalloidin (green) were used to stain the nuclei and actin filaments, respectively. The cells were then imaged by CLSM. Image J (NIH, Bethesda, MD, USA) was used to quantify immunofluorescence staining [28].

2.23. H&E and immunofluorescence staining of tissues

Femur bone samples and other organs (liver, heart, lung, kidney, spleen and brain) collected from the different groups were fixed in ice-cold 4% paraformaldehyde for 24 h. Bone samples were decalcified for 3 weeks with 10% ethylene diamine tetraacetic acid (EDTA). Each organ was embedded in paraffin then sliced into 4-μm sections and subjected to haematoxylin and eosin staining. For CD31 and EMCN staining, bone samples were embedded in a mixture of 20% sucrose, 8% gelatine plus 2% PVP and cut into 40-μm sections. Bone sections were incubated with anti-mouse EMCN (eBioscience, 14-5851, 1:100) CD31 (eBioscience, 14-0311, 1:50) and overnight at 4 °C, followed by the respective fluorescence-conjugated secondary antibody. The sections were then treated with mounting medium containing DAPI and observed under a confocal microscope.

2.24. TRAP staining

Mouse tibias were fixed for 1 day in 4% paraformaldehyde and decalcified in 10% EDTA for 3 weeks. Each sample was embedded in paraffin then sliced into 10-μm sections and subjected to TRAP staining. Trabecular bone area and number of osteoclasts were calculated within selected areas using ImageJ software.

2.25. Dynamic histomorphometry analysis

Bone fluorescent-labelling assays were used to analyse dynamic bone formation. To label the bone, 25 mg/kg calcein (Aladdin) dissolved in 2% sodium bicarbonate (Aladdin) solution was injected intraperitoneally into mice 7 and 2 days before sacrifice [15]. After fixing in 10% paraformaldehyde for one day, dehydrated and undecalcified femurs were embedded in methyl methacrylate. The proximal metaphysis was

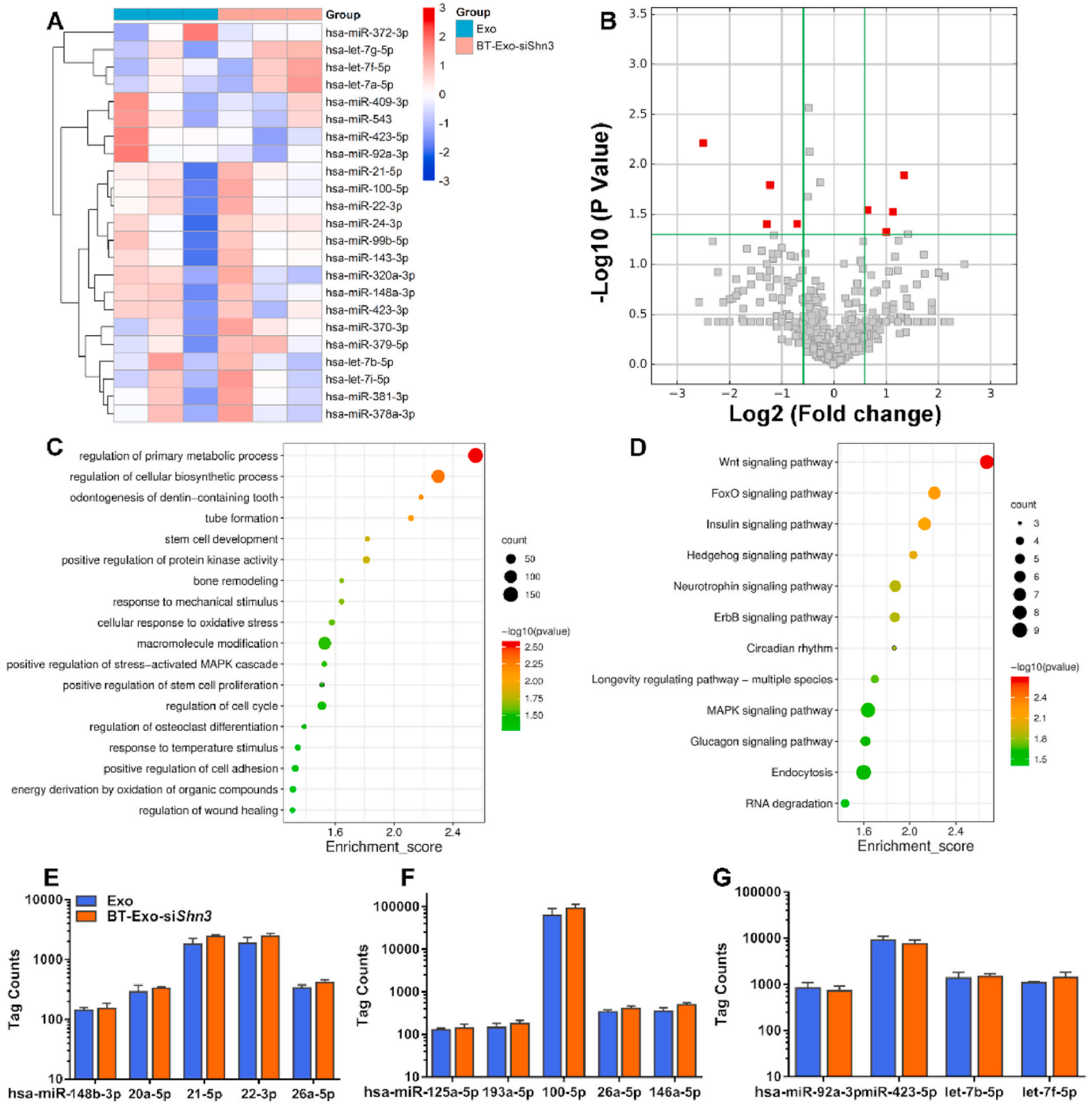

Fig. 2. Endogenous miRNA content of BT-Exo-si*Shn3* and Exos. (A) miRNA Expression profiles of BT-Exo-si*Shn3* and Exo. (B) miRNA expression similarity of BT-Exo-si*Shn3* and Exo shown as a volcano plot. (C) BP enrichment dot plot of endogenous miRNAs by GO analysis. (D) Dot plot of the possible signalling pathways by KEGG analysis. (E–G) Expression of miRNAs involved in promoting osteogenesis (E) and angiogenesis (F), and suppressing osteoclastogenesis (G).

sectioned coronally at 5-mm thickness. The sections were analysed using the OsteoMeasure system (OsteoMetrics Inc., Decatur, GA, USA).

2.26. Microcomputed tomography (μCT) analysis

Femurs were fixed using 4% paraformaldehyde for 1 day and scanned using a Skyscan 1276 (Bruker Corp.). The trabecular region starting from 0.15 mm below the growth plate and extending proximally for 0.4 mm was selected to collect the trabecular bone parameters. The structure image slices were then reconstructed into three-dimensional images.

2.27. Statistical analysis

Numerical data are presented as the mean ± SD. One-way ANOVA for three or more groups and Student's t-test for two groups were performed for statistical analysis using GraphPad Prism 7.0.

3. Results

3.1. Characterization of iMSCs and exosomes

iPSCs were purchased from the Stem Cell Bank, Chinese Academy of

Sciences and then differentiated into iMSCs via established protocols [29]. During the differentiation process, iPSCs lost their typical packed-clones morphology and formed a monolayer with a larger spindle-like appearance (Fig. S1A). Tri-lineage differentiation experiments indicated that the iMSCs exhibited good differentiation potential (Fig. S1B). Flow cytometry (FCM) analysis (Fig. S1C) showed that iMSCs were strongly positive for the surface antigens CD73, CD90 and CD105, and negative for CD14, CD34, CD45, CD79a and HLA-DR. These traits were in accordance with the features of MSCs and demonstrated that iPSCs were successfully differentiated into iMSCs. Thereafter, iMSC-derived exosome (abbreviated as Exo) was isolated from the supernatant of cultured iMSCs. Transmission electron microscopy (TEM) photographs showed that these particles present a typical cup-shape morphology with a size of approximately 100 nm (Fig. S1D). Dynamic light scattering (DLS) and nanoparticle tracking analysis (NTA) revealed that the mean diameter of Exo was 99.8 ± 34 nm (Figs. S1E and S2). Western blotting results confirmed that the specific protein markers Alix, CD81, CD63 were highly expressed in Exo (Fig. S1F). These data indicate that Exo were successfully isolated from the conditioned medium.

3.2. Preparation and characterization of BT-Exo-siShn3

For the bone-targeting modification of Exo (abbreviated as BT-Exo), Exo were conjugated with the peptide SDSSD (Ser, Asp, Ser, Ser, Asp) through a diacyllipid insertion method [30]. To verify the successful modification of Exo, the carboxyl terminal of the peptide was labelled with a FITC fluorophore. Immunomagnetic beads conjugated with CD63 antibodies were used to capture the modified Exos. A strong FITC fluorescence observed using fluorescence microscopy (Fig. 1A) revealed that the bone-targeting peptide SDSSD was successfully anchored onto the surface.

Next, small RNA molecules were loaded into Exo using electroporation technology. To better characterize the successful loading of si*Shn3* at the nanoscale, immunomagnetic beads were used to capture the BT-Exo loaded with Cy3 labelled si*Shn3*. A strong Cy3 fluorescence observed using fluorescence microscopy (Fig. 1D) revealed that the si*Shn3*-Cy3 were successfully loaded into BT-Exo. The morphology of BT-Exo and BT-Exo-si*Shn3* were photographed by TEM, and both exhibited a saucer-like morphology (Fig. 1B and E and S3). The distribution of particle size was detected by DLS. The average diameter of BT-Exo and BT-Exo-si*Shn3* was 108 ± 37 and 118 ± 42 nm, respectively (Fig. 1C and F). Physiological stability of nanocarriers is of significant importance in the application of siRNA delivery. To determine the stability of BT-Exo-si*Shn3* under physiological conditions, we monitored the particle diameter and zeta potential in 50% foetal bovine serum (FBS) for 7 consecutive days by DLS [31]. The hydrodynamic diameter of BT-Exo-si*Shn3* was slightly changed from 114.6 ± 2.2 nm to 121.4 ± 4.0 nm, while the surface zeta potential fluctuated from −16.8 ± 1.8 mV to −21.3 ± 2.1 mV (Fig. 1G). These results indicated that BT-Exo-si*Shn3* had stable physical characteristics.

Providing protection for siRNA from degradation is an important reason for the choice of exosomes as a delivery system. To detect the tolerance of serum-mediated siRNA degradation, BT-Exo-si*Shn3*, Exo-si*Shn3* and naked si*Shn3* were incubated with FBS for a series of time intervals [32]. As shown in Fig. 1H, the band representing naked siRNA disappeared after incubation for 4 h, while si*Shn3* encapsulated in BT-Exo and Exo alone were still detectable at 16 h. These results demonstrated that the membranes of Exo maintained their integrity and consequently protected siRNA from nucleases in FBS after modification and electroporation.

To determine the loading efficiency and release kinetics of loaded RNA, Cel-miRNA-67 (miRNA derived from *Caenorhabditis elegans*, not expressed in mammals) was chosen as the counterpart of si*Shn3* to minimize the experimental background [24]. The miRNA loading efficiency of BT-Exo determined by Q-PCR was 18% (Fig. S4). After incubation for 2 h, Cel-miRNA-67 efflux was approximately 11% in phosphate-buffered saline (PBS) and 9% in 50% FBS. After incubation for 24 h, the release saturated at about 95% in PBS and 98% in FBS (Fig. 1I). After these manipulations, the results of western blotting confirmed that the final engineered nanoparticles still retained the protein marker of exosomes (Fig. S5). CCK-8 assays indicated that the engineered exosomes possessed parallel biosecurity with natural exosomes (Fig. S6).

3.3. Endogenous miRNA content of BT-Exo-siShn3 and Exo

It is well accepted that exosomes function as regulators of recipient cells by delivering proteins, mRNAs, or miRNAs. Recently, the miRNAs of exosomes have raised great concern because they have been shown to influence multiple signalling pathways [33]. Exosomes secreted by iMSCs have been reported to enhance angiogenesis and osteogenesis [21,22,34], but the miRNA content of these exosomes is still unclear. Loading of RNA cargos into exosomes by electroporation and membrane-anchored modification methods were used to develop novel drug delivery systems (DDSs) [24,35]. However, whether the artificial operations would change the endogenous miRNA content of exosomes was not investigated.

To determine the endogenous miRNA content and the influence of electroporation and modification, next-generation sequencing (NGS) was conducted. Thousands of miRNAs were analysed by NGS. The expression profiles are shown in Fig. 2A and B. Compared to the Exo group, there was no significant difference in the miRNAs expressed by BT-Exo-si*Shn3* (Fig. 2B and Fig. S7). Both of them showed the same expression of the most abundant miRNAs, which indicated that the electroporation and modification had no influence on the endogenous miRNAs carried by Exo. Next, we performed Gene Ontology (GO) and Kyoto Encyclopaedia of Genes and Genomes (KEGG) enrichment analyses to clarify the biological processes and pathways potentially involved. Biological process (BP) results of GO analysis (Fig. 2C) showed that these miRNAs mainly regulate primary metabolic processes, cellular biosynthetic processes, macromolecule modification and cell cycle. Some BPs directly related to bone metabolism were also involved, such as stem cell development, positive regulation of protein kinase activity, response to mechanical stimulus, regulation of osteoclast differentiation and positive regulation of stem cell proliferation. Some were directly related to tube formation, wound healing and cellular response to oxidative stress. The majority of the concerned biological processes are known to have regenerative or positive effects. Results of KEGG analysis (Fig. 2D) revealed the pathways to which most of these miRNAs were related. In the top 12 related pathways, Wnt, FoxO and MAPK signalling pathways are closely related to osteogenesis and angiogenesis.

More importantly, osteogenic miRNAs, such as Hsa-miR-148b-3p [36], Hsa-miR-20a-5p [37], Hsa-miR-21-5p [38,39], has-miR-22-3p [40] and has-miR-26a-5p [41] were highly expressed in these Exo (Fig. 2E). According to previous studies, these miRNAs might promote the osteogenic commitment of MSCs or increase the activity of osteoblasts. In addition, osteoclast inhibitory miRNAs were more abundant in the Exo, such as has-miR-100-5p [42], has-miR-125a-5p [43], has-miR-26a-5p [44] and has-miR-146a-5p [45]. These miRNAs could inhibit osteoclast differentiation and activity (Fig. 2F). Moreover, proangiogenic miRNAs also showed high levels of expression, such as has-miR-92a-3p [46], has-miR-423-5p [47], has-miR-21-5p [48], has-let-7b-5p [49] and has-let-7f-5p [50]. These miRNAs were found to improve neovascularization (Fig. 2G).

3.4. Bone-targeting capability in vitro and vivo

The bone-targeting-moiety SDSSD peptide binds to periostin in a ligand–receptor specific manner for osteoblast targeting [51]. It is well known that osteoblasts are derived from MSCs and that the markers of

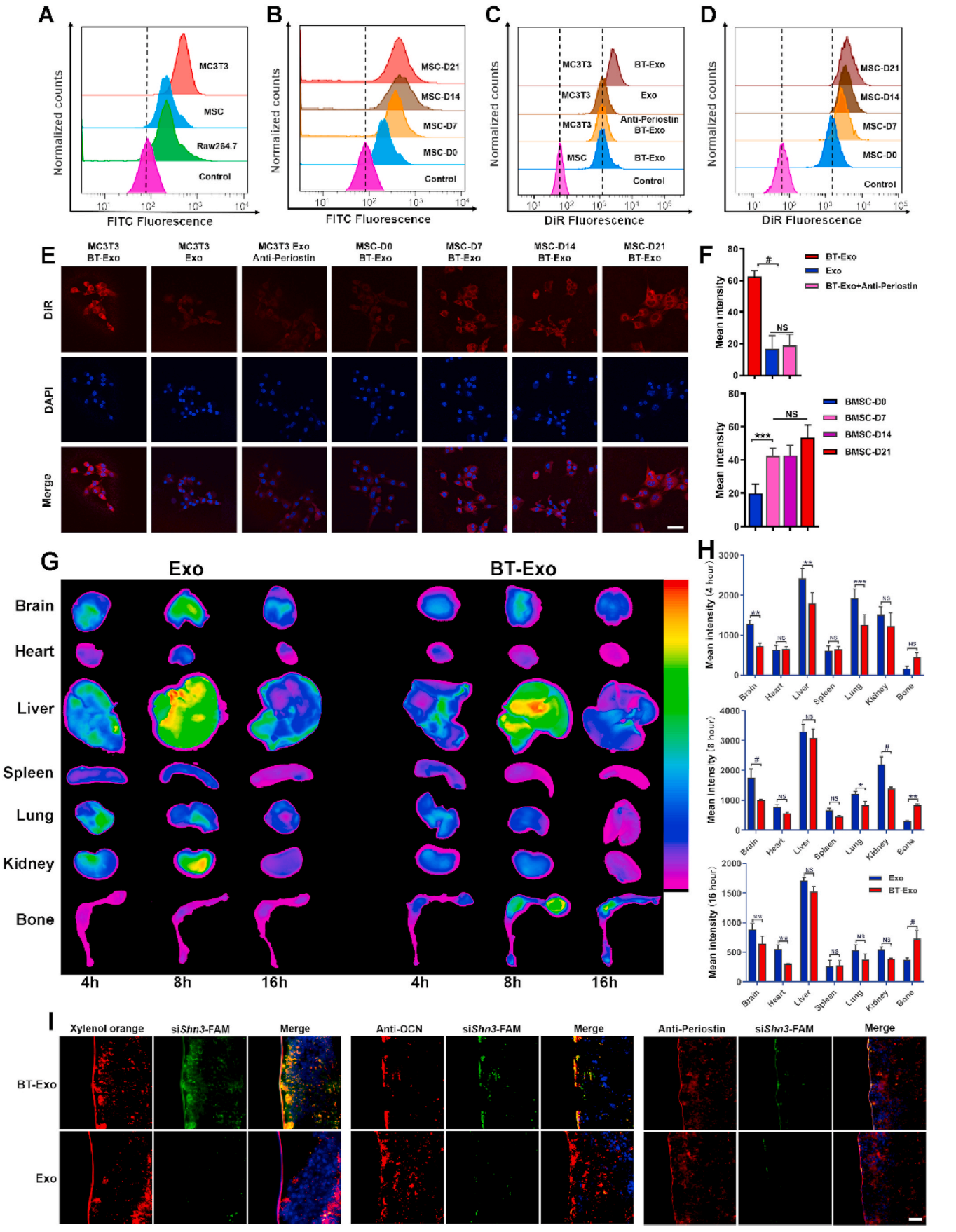

(caption on next page)

Fig. 3. Bone-targeting capability *in vitro* and *vivo*. (A) FCM analysis of periostin expression on the surface of MC3T3 cells, MSCs and Raw 264.7 cells. (B) Periostin expression on the surface of MSCs during osteogenic induction. (C) Uptake of DiR labelled BT-Exo or Exo detected by FCM in MC3T3 cells and MSCs. Anti-periostin antibody was used to block the specific binding in MC3T3 cells. The fluorescence was stronger in the MC3T3 cells incubated with BT-Exo than in other groups. (D) Uptake of DiR-labelled BT-Exo by MSCs during the different stages of osteogenic induction. (E) Uptake of DiR-labelled BT-Exo or Exo detected by CLSM. Scale bar = 20 μm. (F) Quantification of DiR fluorescence intensity. (G) Biodistribution of DiR-labelled BT-Exo-si*Shn3* or Exo-si*Shn3* in mouse. (H) Fluorescence intensity of DiR-labelled BT-Exo-si*Shn3* or Exo-si*Shn3* in different organs. (I) Localization of siRNA-FAM to bone formation surfaces, osteoblasts and periostin delivered by BT-Exo or Exo. Scale bar = 20 μm. (NS, no significant difference; *, $p < 0.05$; **, $p < 0.01$; ***, $p < 0.001$; #, $p < 0.0001$).

osteoblast lineage change during the differentiation process [52]. Based on this consensus, we subsequently investigated the expression of periostin and confirmed that periostin was highly expressed on the membrane of osteoblasts compared with endothelial cells (ECs) and MSCs, as shown in Fig. 3A. Furthermore, increased expression of periostin on the membrane of MSCs was detected during the osteogenic induction process, as shown in Fig. 3B.

To examine whether osteoblasts could take up BT-Exo in a periostin-dependent manner, DiR-labelled BT-Exo or non-bone-targeting Exo were incubated with cells for 2 h. As illustrated in Fig. 3C, stronger fluorescent signals were observed using flow cytometry in BT-Exo-treated osteoblasts compared to MSCs and non-bone-targeting Exo. To further confirm that the SDSSD peptide could enhance osteoblast uptake, MSCs were preincubated with periostin antibody to block periostin. Reduced uptake of BT-Exo was observed compared with cells not pre-incubated with antibody. Further, more uptake of BT-Exo was observed during the osteogenic induction process of MSCs (Fig. 3D). Correspondingly, osteoblast-specific uptake was further confirmed using confocal laser scanning microscopy (CLSM) (Fig. 3E and F). Moreover, we investigated the BT-Exo-mediated knockdown effect by interfering relatively constant GAPDH because the *Shn3* gene expression of different cells were not on the same baseline. The results of Western blot assay also indicated that the engineered exosomes showed stronger knockdown effect in osteoblasts than in endothelial cells and Raw 264.7 (Fig. S8).

The bone targeting ability of BT-Exo was further investigated *in vivo*. The bone accumulation of Exo was evaluated using biophotonic imaging after intravenous injection of DiR-labelled BT-Exo-si*Shn3* or Exo-si*Shn3* into mice. The major organs (brain, heart, liver, spleen, lungs, kidneys, tibia and femur) were harvested for imaging. A stronger fluorescent signal was observed in the bone of BT-Exo-si*Shn3*-treated mice compared to Exo-si*Shn3*-treated animals (Fig. 3G). The fluorescence signal intensity was recorded for quantitative analysis, as shown in Fig. 3H, which revealed that modification with SDSSD may facilitate bone accumulation of exosomes and reduce their biodistribution in other organs. This was consistent with a previous study using SDSSD-modified polyurethane nano micelles [51].

Next, we investigated the osteoblast-targeted delivery ability of BT-Exo-si*Shn3*. First, we labelled bone-forming surfaces with xylenol orange (an orange-red fluorescent substance which binds preferentially to active mineralization areas of newly-formed bone) and traced the si*Shn3*-FAM with green fluorescence. Abundant colocalization of red and green fluorescence was found with BT-Exo-si*Shn3*, whereas little of such colocalization was observed in the Exo-si*Shn3*-treated group (Fig. 3I, left panel). This result revealed that BT-Exo-si*Shn3* delivered si*Shn3* to bone-forming surfaces. Finally, we investigated whether BT-Exo could deliver si*Shn3* to osteoblasts *in vivo*. A marker of mature osteoblasts, OCN, was used to label osteoblasts [53]. As above, many areas of colocalization of si*Shn3* and osteoblasts were observed in the BT-Exo-si*Shn3* group, while few were seen in the Exo-si*Shn3* groups (Fig. 3I, middle panel). Furthermore, the colocalization of si*Shn3* with periostin (Fig. 3I, right panel) confirmed that the osteoblast-specific delivery ability was periostin-dependent.

3.5. BT-Exo-siShn3 promotes osteogenesis and angiogenesis in vitro

The BT-Exo-mediated gene silencing effect constituted an important point of comprehensive anti-osteoporosis effects, and the Western blot assay was used to assess the SHN3 protein expression. These results indicated that BT-Exo-si*Shn3* showed parallel strong gene silencing effect with commercial transfection reagents Lipofectamine 3000 in MC3T3 cells (Fig. S9). In addition, natural exosomes Exo-si*Shn3* also showed obvious silencing effect, which implied that the bone-targeted modification may show more importance *in vivo*. Whereafter, the osteogenic performance of BT-Exo-si*Shn3* was analysed using Alizarin red S (ARS) staining. MC3T3 cells in non-osteo-inductive medium (NOIC) served as negative control, which generated no mineralized nodules. In contrast in osteo-inductive medium (OIC), mineralized nodules of each group were observed qualitatively using microscopy and quantitatively analysed (Fig. 4A and B). On day 7, no significant difference in the formation of calcium nodules was exhibited between any of the groups. On day 14, MC3T3 cells incubated with the BT-Exo-si*Shn3* showed more mineralized matrix than other groups. The BT-Exo and BT-Exo-siCon (random sequence of si*Shn3* loaded in BT-Exo) groups showed obvious increases in the formation of mineralized nodules compared to the PBS and SDSSD groups. The SDSSD group was used to prove that the peptide SDSSD alone had no effect on the cells. On day 21, all the groups in OIC medium showed obvious formation of red-stained mineralized nodules, and the BT-Exo-si*Shn3* group showed the best osteogenic performance. Alkaline phosphatase (ALP) is a marker of early osteogenic differentiation [54], so we analysed ALP activity in the early differentiation stage (Fig. 4C). In accord with the ARS staining, the NOIC medium group showed very low levels of ALP activity throughout the whole process. Meanwhile in the groups in OIC medium, ALP activity started at the same level on day 1 but increased gradually. The BT-Exo-si*Shn3* group exhibited higher ALP activity compared to the other groups. The BT-Exo and BT-Exo-siCon groups showed a moderate increase of ALP activity but exceeded that of the PBS and SDSSD groups. The results verified that the carrier itself has an intrinsic osteogenic effect, which was consistent with previous studies [34], and that loading with si*Shn3* magnified the effect.

Next, the relative mRNA expressions of the osteogenic-related genes runt-related transcription factor 2 (Runx2), osterix (OSX), osteocalcin (OCN), and osteopontin (OPN) were determined by RT-PCR after incubating in OIC medium for 7 days. The overall trend of gene expression was in accord with the staining results (Fig. 4D). Concomitantly, the representative proteins of osteogenic differentiation, OSX and OCN were detected using immunofluorescent staining. When cultured in NOIC medium, the cells showed no expression of these proteins, while all the groups in OIC medium showed observable expression of these osteogenic markers. The trend of protein production was in accord with the results of gene expression analysis and ARS staining (Fig. 4E and F).

Previous studies have shown that SHN3 protein inhibits osteogenesis of osteoblasts and production of the proangiogenic factor SLIT3 [14]. In addition, the most recent study showed that osteoblasts, rather than osteoclasts, are a main source of SLIT3 [55]. Therefore, *Shn3* gene silencing of osteoblasts could theoretically facilitate the production of SLIT3 and tube formation by endothelial cells (ECs). To clarify whether the inhibition of SHN3 could ameliorate the suppression of SLIT3 and promote angiogenesis, we examined the levels of secreted SLIT3 in the supernatant using pre-osteoblasts and ECs in a coculture system under different treatments (Fig. 4G). The supernatant of the BT-Exo-si*Shn3* group showed higher levels of SLIT3 compared with others (Fig. 4H). These results confirmed that the SHN3 gene silencing of osteoblasts increased the production of SLIT3. Then, we assessed the angiogenic activities of ECs after coculture. Compared with the PBS control, tube

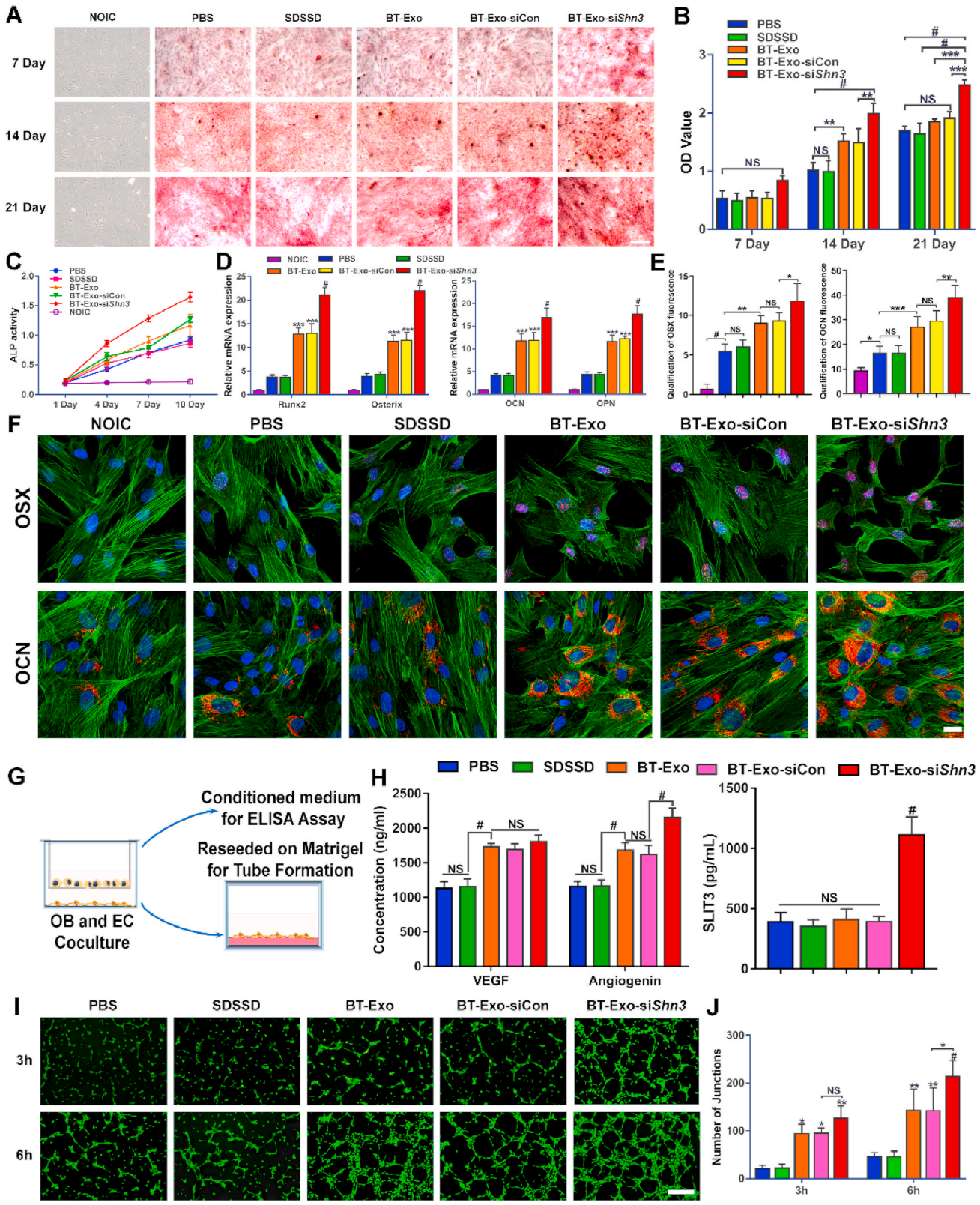

Fig. 4. BT-Exo-si*Shn3* promote osteogenesis and angiogenesis *in vitro*. (A) Representative microscopic images showing mineralized matrix by ARS staining. (B) Quantitative analysis of ARS staining. (C) ALP activity of cells incubated with different nano-particles in normal NOIC medium and OIC medium on days 1, 4, 7 and 10. (D) Relative mRNA expression of osteogenesis-related genes (Runx2, OSX, OCN and OPN) after incubation with different nano-particles for 7 days in NOIC and OIC medium. (E) Bar graph data showing the fluorescence intensity of OSX and OCN. (F) Representative immunofluorescent images showing expression of osteogenic differentiation-related proteins (OSX and OCN) by MC3T3 cells after different treatments for 10 days. (G) Schematic illustration of pre-osteoblasts and EC coculture assays. (H) Expression level of VEGF, angiogenin and SLIT3 in the coculture system after different treatments. (I) Representative fluorescence images showing the tube formation of bEND.3 cells at 3 and 6 h. Scale bar = 100 μm. (J) Bar graph data showing the number of junctions in the tube network of bEND.3 cells after different treatments. (NS, no significant difference; *, $p < 0.05$; **, $p < 0.01$; ***, $p < 0.001$; #, $p < 0.0001$).

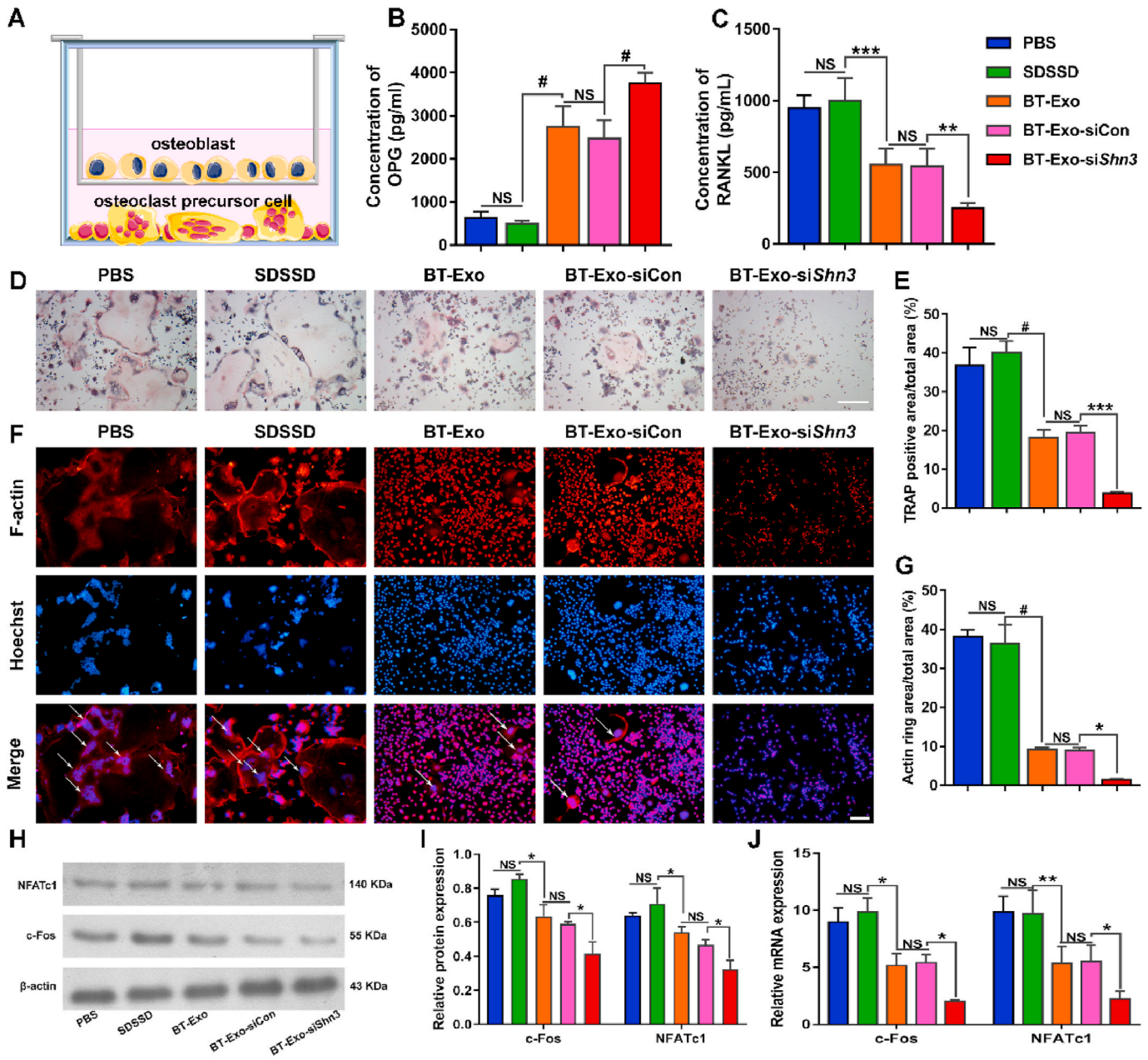

Fig. 5. BT-Exo-si*Shn3* inhibit osteoclastogenesis *in vitro*. (A) Schematic illustration of pre-osteoblasts and osteoclast precursors. (B–C) The expression levels of RANKL and OPG in the coculture system after different treatments. (D) Microscopic images of TRAP staining of Raw264.7 cells in the lower chamber, scale bar = 200 μm. (E) Quantitative analysis of the ratio of TRAP-positive areas to total areas. (F) Representative images of F-actin staining. Scale bar = 100 μm. (G) Quantitative analysis of the ratio of F-actin ring areas to total areas. (H–I) Osteoclastogenesis-related protein (c-Fos and NFATc1) expression analysed by Western blot assay. (J) Osteoclastogenesis-related gene (c-Fos and NFATc1) expression analysed by PCR. (NS, no significant difference; *, $p < 0.05$; **, $p < 0.01$; ***, $p < 0.001$; #, $p < 0.0001$).

formation by ECs appeared no different from the SDSSD group, was moderately enhanced in the BT-Exo-siCon and BT-Exo groups and obviously enhanced in the BT-Exo-si*Shn3* group (Fig. 4I and J and S10). These results indicated that the peptide SDSSD had no effect on angiogenesis while the Exos alone promoted tube formation by ECs, which supports previous reports [21,22]. When loaded with si*Shn3*, BT-Exo-si*Shn3* demonstrated stronger induction of angiogenesis compared with BT-Exo-siCon. To elucidate the intrinsic angiogenic effect of Exo, we analysed the concentration of other angiogenic factors using an ELISA kit. The results showed that VEGF and angiogenin showed higher concentration in all Exo-containing groups (Fig. 4H), which may explain the intrinsic angiogenic effect of Exo.

3.6. BT-Exo-siShn3 inhibits osteoclastogenesis in vitro

Osteoblastic cells including MSCs, osteoblasts and osteocytes drive osteoclast development by secreting RANKL when supplemented with prostaglandin E_2 (PGE_2) and 1,25-dihydroxyvitamin D_3 ($1,25(OH)_2D_3$) [26]. Previous studies have shown that SHN3 inhibition of osteoblasts results in reduced levels of RANKL expression and inability to support osteoclast formation [13]. To clarify whether the BT-Exo-si*Shn3* treatment of osteoblasts caused concomitant suppression of osteoclastogenesis, we performed coculture experiments using pre-osteoblasts and the osteoclast precursors Raw264.7 cells (Fig. 5A). First, we examined the concentrations of RANKL and OPG in the supernatant of coculture systems after incubation with different Exo. The results showed that the

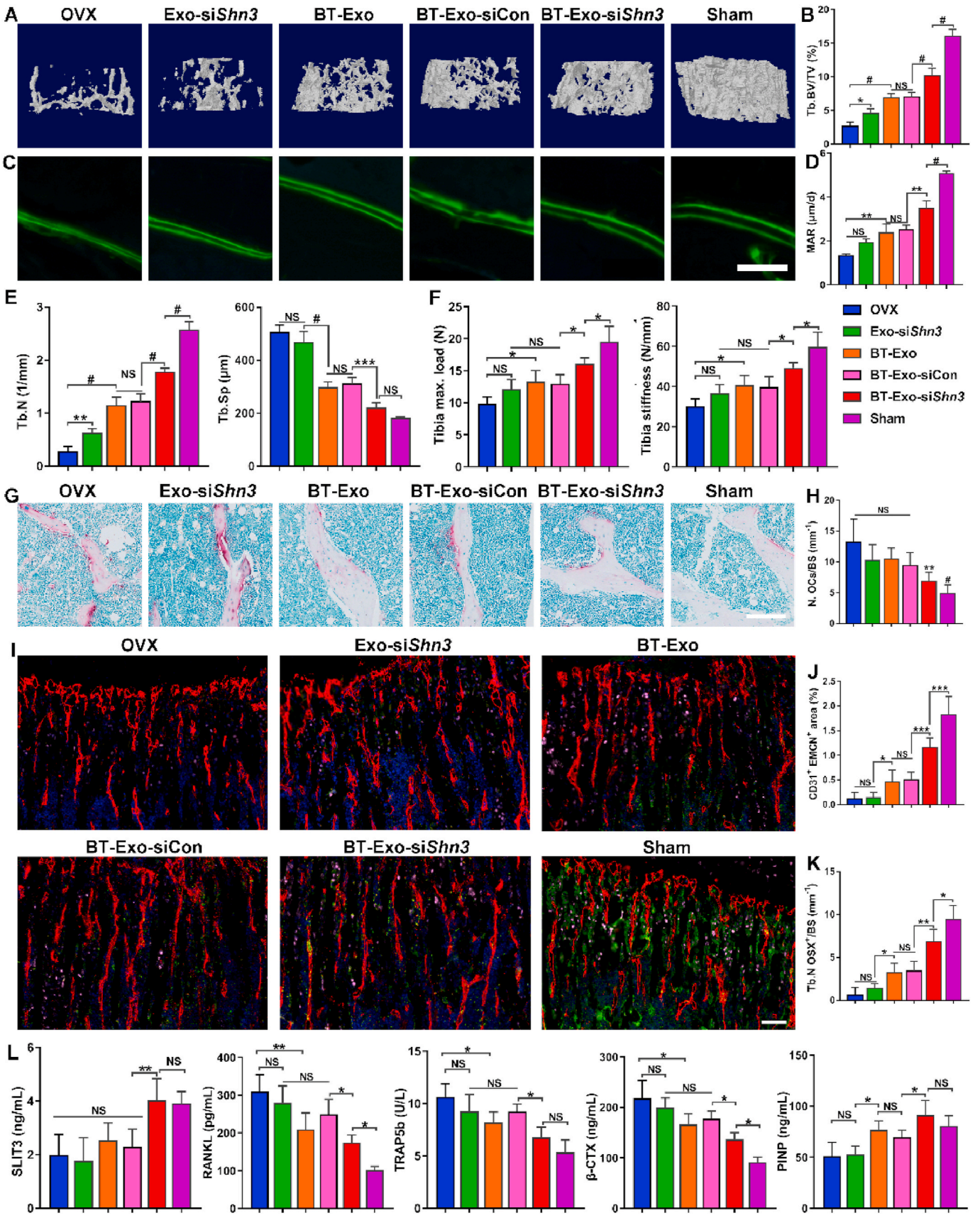

(caption on next page)

Fig. 6. BT-Exo-si*Shn3* promote type H vessel formation and prevent OVX-induced bone loss *in vivo*. (A) Representative micro-CT images showing three-dimensional microarchitecture of trabeculae in the distal femurs. (B) Quantitative analysis of trabecular bone volume per tissue volume (BV/TV). (C) Representative microscopic images showing calcein double labelling of trabecular bone, scale bar = 100 μm. (D) Quantitative analysis of mineral apposition rate (MAR). (E) Quantitative analysis of trabecular number (Tb. N) and trabecular separation (Tb. Sp). (G) Representative photographs of tibias with TRAP staining, scale bar = 100 μm. (H) Histomorphometric analysis of the number of osteoclasts (N. OCs). (I) Representative immunofluorescent images of type H vessels, EMCN (red), CD31 (green), OSX (pink) and nuclei, DAPI (blue). Scale bar = 100 μm. (J–K) Quantitative analysis of type H vessels and osteoprogenitors in distal femurs. (L) Quantitative analysis of serum SLIT3, RANKL, TRAP5b, β-CTX and PINP concentration. (NS, no significant difference; *, $p < 0.05$; **, $p < 0.01$; ***, $p < 0.001$; #, $p < 0.0001$). (For interpretation of the references to colour in this figure legend, the reader is referred to the Web version of this article.)

BT-Exo-si*Shn3* group secreted higher levels of OPG but lower levels of RANKL compared with others (Fig. 5B–C). Then we assessed the effect of osteoclastogenesis using tartrate-resistant acid phosphatase (TRAP) staining and F-actin staining (Fig. 5D–G). Compared with the PBS control, the SDSSD group showed favourable osteoclast formation, and the osteoclast formation was moderately reduced in the BT-Exo-siCon and BT-Exo group and obviously reduced in the BT-Exo-si*Shn3*. The results indicated that the peptide SDSSD had no effect on osteoclastogenesis while the Exo carriers inhibited osteoclast formation from Raw264.7 cells, which could be explained by the abundant endogenous miRNAs which negatively regulate osteoclastogenesis [42]. When loaded with si*Shn3*, BT-Exo-si*Shn3* demonstrated stronger inhibitory effects on osteoclastogenesis compared with BT-Exo-siCon. Concomitantly, the proteins and gene expressions representative of osteoclastogenesis, NFATc1 and c-Fos, were detected (Fig. 5H–J). These results were in accord with the TRAP and F-actin staining results.

3.7. BT-Exo-siShn3 prevents OVX-induced bone loss and promotes type H vessel formation in vivo

To investigate whether BT-Exo-si*Shn3* facilitates bone formation and type H vessel formation *in vivo*, we established a bilateral ovariectomy (OVX)-induced bone loss mouse model. The mice were intravenously administered PBS, BT-Exo-si*Shn3*, BT-Exo-siCon or Exo-si*Shn3* once a week for two months. Micro-CT analysis was then used to analyse the microarchitecture of the distal femur (Fig. 6A and B, 6E and S11). The BT-Exo-si*Shn3* group showed improved bone microarchitecture including higher trabecular volume, trabecular number and lower trabecular separation compared to other groups. The BT-Exo-siCon and BT-Exo groups showed better trabecular bone parameters than non-targeting Exo-si*Shn3*-treated mice. These results indicated that bone-targeted delivery is of great significance in the therapy of osteoporosis. In addition, the cortical bone mass was also stimulated in the BT-Exo-si*Shn3* group while the cortical bone thickness of other groups showed no significant difference with the OVX group and significantly reduced cortical bone mass compared with the Sham group (Fig. S12). Furthermore, bone fluorescent-labelling was used to assess dynamic bone formation. The width between the green fluorescent lines represented the bone formation rate and showed the same trend as trabecular bone parameters (Fig. 6C and D). Moreover, the mechanical property results also showed a significant improvement of bone strength in the BT-Exo-si*Shn3* group (Fig. 6F). The BT-Exo-mediated gene silencing of *Shn3* also played a crucial part in the anti-osteoporosis effects *in vivo*, and the Western blot assay was also used to assess whether the BT-Exo-si*Shn3* treatment could decrease SHN3 protein expression of bone tissue. The result confirmed that the bone-targeted engineered exosomes could mediate gene silencing effects *in vivo* (Fig. S13).

To investigate whether BT-Exo-si*Shn3* inhibit osteoclastogenesis *in vivo*, TRAP staining was performed to indicate the osteoclasts on the trabecular bone surface. In OVX mice, osteoclasts dramatically increased but in OVX mice treated with BT-Exo-si*Shn3* osteoclasts distinctly decreased (Fig. 6G and H). These results suggest that BT-Exo-si*Shn3* could inhibit osteoclast formation *in vivo*.

Next, we detected the effects of BT-Exo-si*Shn3* on type H vessel formation using immunofluorescent staining. According to the results (Figure. 6I, 6J–K), the number of $CD31^{high}Emcn^{high}$ ECs and OSX-positive osteoprogenitors in the distal femur of OVX mice was markedly reduced compared to the Sham group, while BT-Exo-si*Shn3* treatment distinctly mitigated the reduction. The groups administered BT-Exo-siCon and BT-Exos showed weaker effects on this, while non-targeting Exo-si*Shn3*-treated mice showed no effect on type H vessel formation or osteoprogenitor recruitment. These results revealed that OVX induced a remarkable decrease of type H vessels and osteoprogenitors, while osteoblast-targeting delivery of si*Shn3* could partially ameliorate this effect. Furthermore, we examined the concentrations of SLIT3, RANKL, and the bone metabolism biochemical indicators in the serum including TRAP5b, β-CTX and PINP (Fig. 6L). These results showed that BT-Exo-si*Shn3* treatment reduced the RANKL production and bone resorption markers (TRAP5b and β-CTX) while increased the SLIT3 secretion and bone formation marker PINP, which were in accord with histomorphometric detection. In addition, no apparent histomorphometric changes were found in the brain, heart, liver, spleen, lung or kidney in each group, indicating that BT-Exo-si*Shn3* treatment was well-tolerated, without obvious systemic toxicity (Fig. S14).

4. Discussion

In this study, we constructed an engineered exosome DDS based on exosomes modified with a bone-targeting peptide, named BT-Exo-si*Shn3*, for osteoporosis therapy. Unlike previously-reported DDS for osteoporosis treatment, BT-Exo-si*Shn3* could deliver si*Shn3* to osteoblasts and bone-forming surfaces specifically via SDSSD/periostin interactions, which was demonstrated using immunofluorescent staining. Wang et al. have previously reported a bone-targeted alendronate combined MSC-derived exosome targeting bone via hydroxyapatite [56]. Luo et al. reported an aptamer-functionalized MSC-derived exosome for osteoporosis treatment [57]. Hu et al. constructed hybrid nanoparticles based on C-X-C motif chemokine receptor 4 (CXCR4)-positive exosomes [58], which took advantage of mechanism involved in the $CXCR4^{+}$ cells homing to implement bone-targeted drug delivery. However, these results only showed the increased bone accumulation rather than delivery to specific bone cells *in vivo*. In addition to this, most published studies [19,20,58] about exosomes for bone regeneration or osteoporosis treatment only showed single mechanism while the BT-Exo-si*Shn3* showed synergistic and comprehensive anti-osteoporosis effects including enhanced osteogenic differentiation, promoted type H vessel formation and inhibited osteoclast formation. Furthermore, most studies [57,58] reported that the effect of exosomes loading siRNA has depended on the siRNA cargo while the exosomes only acted as carriers. In contrast, the BT-Exo-si*Shn3* took advantage of the intrinsic anti-osteoporosis effects of iMSC-derived exosomes and collaborated with the loaded siRNA to enhance the efficacy. It achieved synchronization and unification of carrier and cargo in the BT-Exo-si*Shn3* DDS. Of course, we have to acknowledge that the complexity and technical challenges may limit the clinical transformation of BT-Exo-si*Shn3* DDS at present.

To the best of our knowledge, this study is the first report of a DDS using extracellular vesicles produced by iPSC-derivatives, which can be used for autologous treatment without ethical issues or immunological rejection. Pluripotent stem cells (PSCs), including both human embryonic stem cells (hESCs) and iPSCs, represent the second generation of stem cells. Multipotent somatic stem cells, such as hematopoietic stem cells (HSCs), mesenchymal stem/stromal cells (MSCs) and fetal tissue-derived stem cells are the first-generation stem cell types [59]. Among

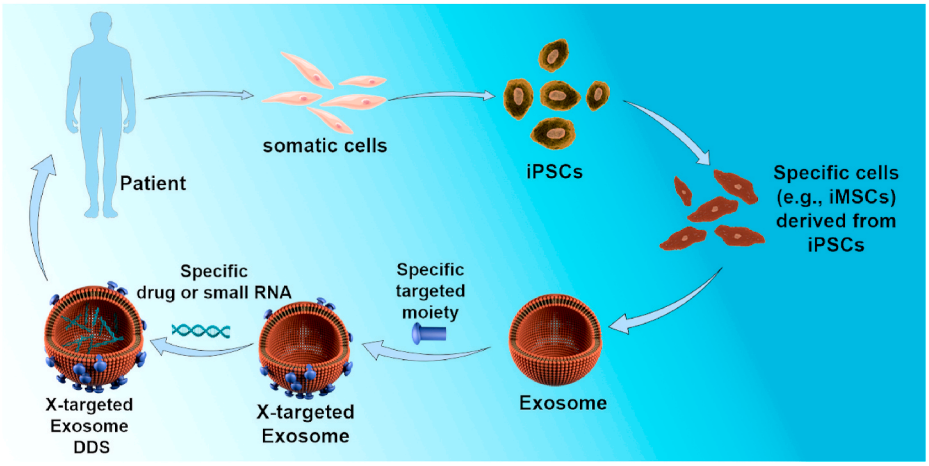

Scheme 2. A versatile paradigm for targeting therapy of specific diseases using an X-targeted exosome DDS.

the first-generation stem cells, MSCs are the most widely applied cells in regenerative medicine. Compared with the second generation, conventional MSCs has a number of limitations. Firstly, the procedures involved in harvesting MSCs from adult tissues are invasive. Secondly, the proliferation and differentiation capacities of MSCs are limited after several passages in culture. Moreover, the proliferation and differentiation potential of MSCs declines significantly with increasing when age-related disorders occur [21]. Among the second-generation stem cells, iPSCs and iPSC-derivatives can be used without ethical hurdles which restrict application of ESCs. iPSCs, generated from most tissues in the body, possess similar self-renewal and differentiation capacity with ESCs type. Nowadays, iPSCs and their derivatives generated using footprint-free induction technology will not have any risks of undesired genomic modifications associated with reprogramming protocol [60]. As the first preclinical study for bone diseases using exosomes produced by iPSC-derivatives, the BT-Exo-si*Shn3* may gain further development when the technology regulation and cost problems are overcome. Inspired by this project, we propose a versatile paradigm of targeted therapy for specific diseases (Scheme 2). Accessible somatic cells can be harvested from patients and converted into iPSCs using induced pluripotent stem cell reprogramming technology. The patient-specific iPSCs can then be differentiated into specific cells (such as iMSCs, endothelial cells or myocardial cells) according to treatment need. The induced specific cells can serve as a factory producing exosomes. Then the exosomes can be modified with different targeting-moieties and loaded with different small molecular drugs or RNA drugs as required. Ultimately, the patient-specific engineered exosomes will be used as specific medication for an individual patient without causing any ethical arguments or risking immunological rejection. In this way, we can construct a versatile DDS, X-targeted exosome, for various diseases using this paradigm and platform.

5. Conclusions

In summary, we constructed a bone-targeted engineered exosome platform BT-Exo-si*Shn3*, which was able to deliver si*Shn3* to osteoblasts specifically. BT-Exo-si*Shn3* took advantage of the intrinsic anti-osteoporosis function of iMSC-derived exosomes and collaborated with the loaded siRNA of the *Shn3* gene to enhance the therapeutic effects. The engineered exosomes may serve as a promising therapy to kill three birds with one stone and implement comprehensive anti-osteoporosis effects.

CRediT authorship contribution statement

Yongzhi Cui: Conceptualization, Methodology, Investigation, Visualization, Formal analysis, Writing – original draft. **Yuanyuan Guo:** Investigation, Methodology, Conceptualization, Visualization, Formal analysis. **Li Kong:** Investigation, Writing – review & editing. **Jingyu Shi:** Investigation, Methodology. **Ping Liu:** Investigation, Methodology. **Rui Li:** Investigation. **Yongtao Geng:** Methodology. **Weihang Gao:** Investigation. **Zhiping Zhang:** Investigation, Supervision. **Dehao Fu:** Investigation, Supervision, Writing – review & editing, Funding acquisition.

Declaration of competing interest

The authors declare no conflict of interest.

Acknowledgement

We thank Shanghai CloudSeq Biotech Company for conducting the small RNA NGS assay and Dr Lin Zeng (BioDataStudio, Shanghai) for bioinformatics analysis. This study was supported by the National Natural Science Foundation of China (Grant No: 81874026 and 82070911).

Appendix A. Supplementary data

Supplementary data to this article can be found online at https://doi.org/10.1016/j.bioactmat.2021.09.015.

References

[1] Consensus development conference: diagnosis, prophylaxis, and treatment of osteoporosis, Am. J. Med. 94 (6) (1993) 646–650.
[2] J.E. Compston, M.R. McClung, W.D. Leslie, Osteoporosis, Lancet 393 (10169) (2019) 364–376.
[3] D.M. Black, C.J. Rosen, Clinical practice. Postmenopausal osteoporosis, N. Engl. J. Med. 374 (3) (2016) 254–262.
[4] C. Brown, Osteoporosis: staying strong, Nature 550 (7674) (2017) s15–s17.
[5] T. Luhmann, O. Germershaus, J. Groll, L. Meinel, Bone targeting for the treatment of osteoporosis, J. Contr. Release 161 (2) (2012) 198–213.
[6] A.P. Kusumbe, S.K. Ramasamy, R.H. Adams, Coupling of angiogenesis and osteogenesis by a specific vessel subtype in bone, Nature 507 (7492) (2014) 323–328.
[7] M. Yang, C.J. Li, X. Sun, Q. Guo, Y. Xiao, T. Su, et al., MiR-497 approximately 195 cluster regulates angiogenesis during coupling with osteogenesis by maintaining endothelial Notch and HIF-1alpha activity, Nat. Commun. 8 (2017) 16003.
[8] L. Wang, F. Zhou, P. Zhang, H. Wang, Z. Qu, P. Jia, et al., Human type H vessels are a sensitive biomarker of bone mass, Cell Death Dis. 8 (5) (2017), e2760.
[9] C. Song, J. Cao, Y. Lei, H. Chi, P. Kong, G. Chen, et al., Nuciferine prevents bone loss by disrupting multinucleated osteoclast formation and promoting type H vessel formation, Faseb. J. 34 (3) (2020) 4798–4811.
[10] M. Yang, C.J. Li, Y. Xiao, Q. Guo, Y. Huang, T. Su, et al., Ophiopogonin D promotes bone regeneration by stimulating CD31hi EMCNhi vessel formation, Cell Prolif 53 (3) (2020), e12784.
[11] J.H. Shim, M.B. Greenblatt, W. Zou, Z. Huang, M.N. Wein, N. Brady, et al., Schnurri-3 regulates ERK downstream of WNT signaling in osteoblasts, J. Clin. Invest. 123 (9) (2013) 4010–4022.

[12] D.C. Jones, M.N. Wein, M. Oukka, J.G. Hofstaetter, M.J. Glimcher, L.H. Glimcher, Regulation of adult bone mass by the zinc finger adapter protein Schnurri-3, Science 312 (5777) (2006) 1223–1227.
[13] M.N. Wein, D.C. Jones, J.H. Shim, A.O. Aliprantis, R. Sulyanto, V. Lazarevic, et al., Control of bone resorption in mice by Schnurri-3, Proc. Natl. Acad. Sci. U. S. A. 109 (21) (2012) 8173–8178.
[14] R. Xu, A. Yallowitz, A. Qin, Z. Wu, D.Y. Shin, J.M. Kim, et al., Targeting skeletal endothelium to ameliorate bone loss, Nat. Med. 24 (6) (2018) 823–833.
[15] Y.S. Yang, J. Xie, D. Wang, J.M. Kim, P.W.L. Tai, E. Gravallese, et al., Bone-targeting AAV-mediated silencing of Schnurri-3 prevents bone loss in osteoporosis, Nat. Commun. 10 (1) (2019) 2958.
[16] M. Lu, Y. Huang, Bioinspired exosome-like therapeutics and delivery nanoplatforms, Biomaterials 242 (2020) 119925.
[17] S. Liu, X. Xu, S. Liang, Z. Chen, Y. Zhang, A. Qian, et al., The application of MSCs-derived extracellular vesicles in bone disorders: novel cell-free therapeutic strategy, Front. Cell. Dev. Biol. 8 (2020) 619.
[18] D.G. Phinney, M.F. Pittenger, Concise review: MSC-derived exosomes for cell-free therapy, Stem Cell. 35 (4) (2017) 851–858.
[19] J. Fan, C.S. Lee, S. Kim, C. Chen, T. Aghaloo, M. Lee, Generation of small RNA-modulated exosome mimetics for bone regeneration, ACS Nano 14 (9) (2020) 11973–11984.
[20] M.Á. Brennan, P. Layrolle, D.J. Mooney, Biomaterials functionalized with MSC secreted extracellular vesicles and soluble factors for tissue regeneration, Adv. Funct. Mater. 30 (37) (2020) 1909125.
[21] J. Zhang, J. Guan, X. Niu, G. Hu, S. Guo, Q. Li, et al., Exosomes released from human induced pluripotent stem cells-derived MSCs facilitate cutaneous wound healing by promoting collagen synthesis and angiogenesis, J. Transl. Med. 13 (2015) 49.
[22] G.W. Hu, Q. Li, X. Niu, B. Hu, J. Liu, S.M. Zhou, et al., Exosomes secreted by human-induced pluripotent stem cell-derived mesenchymal stem cells attenuate limb ischemia by promoting angiogenesis in mice, Stem Cell Res. Ther. 6 (2015) 10.
[23] L. Alvarez-Erviti, Y. Seow, H. Yin, C. Betts, S. Lakhal, M.J. Wood, Delivery of siRNA to the mouse brain by systemic injection of targeted exosomes, Nat. Biotechnol. 29 (4) (2011) 341–345.
[24] Y. Wang, X. Chen, B. Tian, J. Liu, L. Yang, L. Zeng, et al., Nucleolin-targeted extracellular vesicles as a versatile platform for biologics delivery to breast cancer, Theranostics 7 (5) (2017) 1360–1372.
[25] M.J. Jiang, Y.Y. Chen, J.J. Dai, D.N. Gu, Z. Mei, F.R. Liu, et al., Dying tumor cell-derived exosomal miR-194-5p potentiates survival and repopulation of tumor repopulating cells upon radiotherapy in pancreatic cancer, Mol. Canc. 19 (1) (2020) 68.
[26] T. Nakashima, M. Hayashi, T. Fukunaga, K. Kurata, M. Oh-Hora, J.Q. Feng, et al., Evidence for osteocyte regulation of bone homeostasis through RANKL expression, Nat. Med. 17 (10) (2011) 1231–1234.
[27] Y. Yan, H. Chen, H. Zhang, C. Guo, K. Yang, K. Chen, et al., Vascularized 3D printed scaffolds for promoting bone regeneration, Biomaterials 190–191 (2019) 97–110.
[28] M. Zhai, Y. Zhu, M. Yang, C. Mao, Human mesenchymal stem cell derived exosomes enhance cell-free bone regeneration by altering their miRNAs profiles, Adv. Sci. (2020) 2001334.
[29] Y. Xia, X. Ling, G. Hu, Q. Zhu, J. Zhang, Q. Li, et al., Small extracellular vesicles secreted by human iPSC-derived MSC enhance angiogenesis through inhibiting STAT3-dependent autophagy in ischemic stroke, Stem Cell Res. Ther. 11 (1) (2020) 313.
[30] J. Zou, M. Shi, X. Liu, C. Jin, X. Xing, L. Qiu, et al., Aptamer-functionalized exosomes: elucidating the cellular uptake mechanism and the potential for cancer-targeted chemotherapy, Anal. Chem. 91 (3) (2019) 2425–2430.
[31] Y. Guo, D. Wang, Q. Song, T. Wu, X. Zhuang, Y. Bao, et al., Erythrocyte membrane-enveloped polymeric nanoparticles as nanovaccine for induction of antitumor immunity against melanoma, ACS Nano 9 (7) (2015) 6918–6933.
[32] S. He, W. Fan, N. Wu, J. Zhu, Y. Miao, X. Miao, et al., Lipid-based liquid crystalline nanoparticles facilitate cytosolic delivery of siRNA via structural transformation, Nano Lett. 18 (4) (2018) 2411–2419.
[33] X. Yao, W. Wei, X. Wang, L. Chenglin, M. Bjorklund, H. Ouyang, Stem cell derived exosomes: microRNA therapy for age-related musculoskeletal disorders, Biomaterials 224 (2019) 119492.
[34] X. Qi, J. Zhang, H. Yuan, Z. Xu, Q. Li, X. Niu, et al., Exosomes secreted by human-induced pluripotent stem cell-derived mesenchymal stem cells repair critical-sized bone defects through enhanced angiogenesis and osteogenesis in osteoporotic rats, Int. J. Biol. Sci. 12 (7) (2016) 836–849.
[35] S.C. Tao, S.C. Guo, C.Q. Zhang, Modularized extracellular vesicles: the dawn of prospective personalized and precision medicine, Adv. Sci. 5 (2) (2018) 1700449.
[36] K.C. Li, S.C. Lo, L.Y. Sung, Y.H. Liao, Y.H. Chang, Y.C. Hu, Improved calvarial bone repair by hASCs engineered with Cre/loxP-based baculovirus conferring prolonged BMP-2 and MiR-148b co-expression, J. Tissue Eng. Regen. Med. 11 (11) (2017) 3068–3077.
[37] J.F. Zhang, W.M. Fu, M.L. He, W.D. Xie, Q. Lv, G. Wan, et al., MiRNA-20a promotes osteogenic differentiation of human mesenchymal stem cells by co-regulating BMP signaling, RNA Biol. 8 (5) (2011) 829–838.
[38] Y. Sun, L. Xu, S. Huang, Y. Hou, Y. Liu, K.M. Chan, et al., mir-21 overexpressing mesenchymal stem cells accelerate fracture healing in a rat closed femur fracture model, BioMed Res. Int. 2015 (2015) 412327.
[39] N. Yang, G. Wang, C. Hu, Y. Shi, L. Liao, S. Shi, et al., Tumor necrosis factor α suppresses the mesenchymal stem cell osteogenesis promoter miR-21 in estrogen deficiency-induced osteoporosis, J. Bone Miner. Res. 28 (3) (2013) 559–573.
[40] S. Huang, S. Wang, C. Bian, Z. Yang, H. Zhou, Y. Zeng, et al., Upregulation of miR-22 promotes osteogenic differentiation and inhibits adipogenic differentiation of human adipose tissue-derived mesenchymal stem cells by repressing HDAC6 protein expression, Stem Cell. Dev. 21 (13) (2012) 2531–2540.
[41] L. Sun, Z. Li, H. Xue, T. Ma, C. Ren, M. Li, et al., MiR-26a promotes fracture healing of nonunion rats possibly by targeting SOSTDC1 and further activating Wnt/β-catenin signaling pathway, Mol. Cell. Biochem. 460 (1–2) (2019) 165–173.
[42] L. Zhou, H.Y. Song, L.L. Gao, L.Y. Yang, S. Mu, Q. Fu, MicroRNA-100-5p inhibits osteoclastogenesis and bone resorption by regulating fibroblast growth factor 21, Int. J. Mol. Med. 43 (2) (2019) 727–738.
[43] L.J. Guo, L. Liao, L. Yang, Y. Li, T.J. Jiang, MiR-125a TNF receptor-associated factor 6 to inhibit osteoclastogenesis, Exp. Cell Res. 321 (2) (2014) 142–152.
[44] K. Kim, J.H. Kim, I. Kim, J. Lee, S. Seong, Y.W. Park, et al., MicroRNA-26a regulates RANKL-induced osteoclast formation, Mol. Cell. 38 (1) (2015) 75–80.
[45] T. Nakasa, H. Shibuya, Y. Nagata, T. Niimoto, M. Ochi, The inhibitory effect of microRNA-146a expression on bone destruction in collagen-induced arthritis, Arthritis Rheum. 63 (6) (2011) 1582–1590.
[46] N. Bellera, I. Barba, A. Rodriguez-Sinovas, E. Ferret, M.A. Asín, M.T. Gonzalez-Alujas, et al., Single intracoronary injection of encapsulated antagomir-92a promotes angiogenesis and prevents adverse infarct remodeling, J. Am. Heart Assoc. 3 (5) (2014), e000946.
[47] F. Xu, Q. Xiang, J. Huang, Q. Chen, N. Yu, X. Long, et al., Exosomal miR-423-5p mediates the proangiogenic activity of human adipose-derived stem cells by targeting Sufu, Stem Cell Res. Ther. 10 (1) (2019) 106.
[48] L. Qiao, S. Hu, S. Liu, H. Zhang, H. Ma, K. Huang, et al., microRNA-21-5p dysregulation in exosomes derived from heart failure patients impairs regenerative potential, J. Clin. Invest. 129 (6) (2019) 2237–2250.
[49] C. Beltrami, M. Besnier, S. Shantikumar, A.I. Shearn, C. Rajakaruna, A. Laftah, et al., Human pericardial fluid contains exosomes enriched with cardiovascular-expressed MicroRNAs and promotes therapeutic angiogenesis, Mol. Ther. 25 (3) (2017) 679–693.
[50] A. Kuehbacher, C. Urbich, A.M. Zeiher, S. Dimmeler, Role of Dicer and Drosha for endothelial microRNA expression and angiogenesis, Circ. Res. 101 (1) (2007) 59–68.
[51] Y. Sun, X. Ye, M. Cai, X. Liu, J. Xiao, C. Zhang, et al., Osteoblast-targeting-peptide modified nanoparticle for siRNA/microRNA delivery, ACS Nano 10 (6) (2016) 5759–5768.
[52] E. Roeder, B.G. Matthews, I. Kalajzic, Visual reporters for study of the osteoblast lineage, Bone 92 (2016) 189–195.
[53] S.L. Dallas, M. Prideaux, L.F. Bonewald, The osteocyte: an endocrine cell and more, Endocr. Rev. 34 (5) (2013) 658–690.
[54] H.S. Ching, N. Luddin, I.A. Rahman, K.T. Ponnuraj, Expression of odontogenic and osteogenic markers in DPSCs and SHED: a review, Curr. Stem Cell Res. Ther. 12 (1) (2017) 71–79.
[55] N. Li, K. Inoue, J. Sun, Y. Niu, S. Lalani, A. Yallowitz, et al., Osteoclasts are not a source of SLIT3, Bone Res. 8 (2020) 11.
[56] Y. Wang, J. Yao, L. Cai, T. Liu, X. Wang, Y. Zhang, et al., Bone-targeted extracellular vesicles from mesenchymal stem cells for osteoporosis therapy, Int. J. Nanomed. 15 (2020) 7967–7977.
[57] Z.W. Luo, F.X. Li, Y.W. Liu, S.S. Rao, H. Yin, J. Huang, et al., Aptamer-functionalized exosomes from bone marrow stromal cells target bone to promote bone regeneration, Nanoscale 11 (43) (2019) 20884–20892.
[58] Y. Hu, X. Li, Q. Zhang, Z. Gu, Y. Luo, J. Guo, et al., Exosome-guided bone tar-geted delivery of Antagomir-188 as an anabolic therapy for bone loss, Bioact. Mater. 6 (9) (2021) 2905–2913.
[59] E.A. Kimbrel, R. Lanza, Next-generation stem cells-ushering in a new era of cell-based therapies, Nat. Rev. Drug Discov. 19 (7) (2020) 463–479.
[60] V. Sabapathy, S. Kumar, hiPSC-derived iMSCs: NextGen MSCs as an advanced therapeutically active cell resource for regenerative medicine, J. Cell Mol. Med. 20 (8) (2016) 1571–1588.